


## Reaction dynamics of the $^{12}\text{C} + ^{181}\text{Ta}$ system near the Coulomb barrier: Evidence of fusion-fission events

Pavneet Kaur <sup>1</sup>, Moumita Maiti <sup>1,\*</sup>, T. N. Nag,<sup>2</sup> and S. Sodaye<sup>2</sup>

<sup>1</sup>*Department of Physics, Indian Institute of Technology Roorkee, Roorkee-247667, Uttarakhand, India*

<sup>2</sup>*Radiochemistry Division, Bhabha Atomic Research Centre, Mumbai-400085, India*

 (Received 18 October 2021; revised 3 December 2021; accepted 11 January 2022; published 31 January 2022)

**Background:** Interaction of a heavy projectile with a heavy target produces a massive compound nucleus (CN), which deexcites through two possible modes: evaporation of light particles and fission. In order to develop a clear understanding of fusion-fission (FF) dynamics, it is important to explore the preactinide region at energies around and above the Coulomb barrier.

**Purpose:** The objective is to study the dynamics involved in the fusion of  $^{12}\text{C}$ , a cluster structured projectile, with  $^{181}\text{Ta}$  target, at energies within 4.3–6.0 MeV/nucleon, by measuring the production cross sections of the radionuclides formed through complete/incomplete fusion (CF/ICF) and fission processes. In addition, the mass distribution of fission fragments, which is an important fission observable, is probed for a better understanding of dynamics.

**Method:** Tantalum foil, backed by the aluminum catcher, arranged in a stack, was bombarded by  $^{12}\text{C}$  ions of 52–73 MeV energy. The off-beam  $\gamma$ -ray spectrometry method was adopted to measure the activity of the residues produced in each Ta target after the end of bombardment (EOB), and cross sections were calculated. To analyze the experimental cross sections, PACE4 and EMPIRE3.2.2 reaction model codes were employed. Further, the mass distribution of fission fragments was explored to obtain mass variance information.

**Results:** In general, measured excitation functions of the residues produced through the evaporation of particles in  $^{12}\text{C} + ^{181}\text{Ta}$  reaction showed good agreement with the predictions of PACE4. ICF of  $^{12}\text{C}$  in  $^{181}\text{Ta}$  target with strength up to 7.7% has been observed and compared with the strength deduced from previously reported data for the same system. However, no signature of precompound processes has been observed in this study. A total of 12 fission fragments within  $71 \leq A \leq 135$  mass range have been identified. Further, mass variance is rising with increasing mass asymmetry, which hints at the importance of entrance-channel parameters' role in deciding the spread of the mass distribution.

**Conclusions:** Good agreement of PACE4 with the excitation functions of  $xn$  channel evaporation residues confirms their production through the CF mechanism. Enhancement of cross sections in the  $\alpha xn$  channel is attributed to the ICF process. Further, evidence of the production of fission fragments through a compound nuclear mechanism is indicated as a broad and symmetric mass distribution, observed through the Gaussian fitting. The trend of mass variance with rising excitation energy and mass asymmetry is found to be growing.

DOI: [10.1103/PhysRevC.105.014629](https://doi.org/10.1103/PhysRevC.105.014629)

### I. INTRODUCTION

Developments in accelerator technology have made it possible to accelerate heavy ions ( $A > 4$ ) and added new opportunities to explore the dynamics of heavy interacting partners. Such reactions involve a large number of nucleons, leading to several new nuclear reaction processes depending upon the energy carried by the projectile and entrance-channel parameters. Several nuclear reaction processes that have been traced in the existing literature [1] on heavy-ion-induced reactions involve (i) complete fusion, the most dominating process, in which the whole projectile fuses with the target, (ii) preequilibrium (PEQ) emissions in which fast light particles are emitted prior to the thermodynamic equilibrium of the composite system, (iii) incomplete fusion in which the

projectile breaks up, and only a part of it gets fused with the target, and (iv) nucleon transfer.

The ICF phenomena have been investigated in case of weakly bound stable ( $^6\text{Li}$ ,  $^9\text{Be}$ ,  $^{10,11}\text{B}$ ) and unstable ( $^{11}\text{Li}$ ,  $^{11}\text{Be}$ ,  $^8\text{B}$ ) projectiles even at low projectile energies,  $\approx 4$ –8 MeV/nucleon, where major part of the reaction cross section was expected from CF process [2–13]. Several experiments involving  $\alpha$ -clustered projectiles have also been performed, which include  $^{12}\text{C}$  on  $^{175}\text{Lu}$  [14],  $^{115}\text{In}$  [15],  $^{159}\text{Tb}$  [16],  $^{169}\text{Tm}$  [17], and  $^{165}\text{Ho}$  [18,19] targets. The occurrence of ICF in these systems has been explained on the basis of low  $\alpha$  separation energy in the case of  $^{12}\text{C}$  projectile that leads to its breakup into  $^8\text{Be}$  and  $\alpha$ . Along with this, strong influence of entrance-channel parameters, such as (i) projectile energy ( $E_{\text{lab}}$ ), (ii) input angular momenta, (iii) mass asymmetry, (iv) Coulomb effect, and (v)  $Q_\alpha$  values of projectiles, on ICF also have been reported at energies below 8 MeV/nucleon [5,20–23]. Although some theoretical models

\*Corresponding author: [moumita.maiti@ph.iitr.ac.in](mailto:moumita.maiti@ph.iitr.ac.in)

have been explored to understand the ICF dynamics, but none of them gave satisfactory reproduction of ICF in this energy range. Hence, experimental exploration of ICF dynamics still carries great interest around the Coulomb barrier.

The study of heavy-ion-induced reactions with heavy-mass targets around the Coulomb barrier is the talking point and necessity at present, especially at the preactinide region due to the lack of experimental studies. Hence, more experimental data are required to understand the reaction dynamics in this particular region. The use of heavy-mass ( $A > 120$ ) targets in the fusion reaction leads to the formation of a massive equilibrated CN that tends to deexcite through two possible routes, evaporation of particles and fission. Thus, the fission process starts contributing along with the fusion in this situation. Extensive studies have been reported for FF dynamics in the actinide region, but those in the sub-lead region are limited. We have made an effort to add some valuable information on the mechanisms involved in the fusion of two massive nuclei ( $^{12}\text{C} + ^{181}\text{Ta}$ ).

Based on previous studies, it has been assumed that fission is grossly originating through the CF process, and a tiny contribution may be through ICF within the energy range of interest [24,25]. Large angular momentum transfer by the projectile results in lowering of the fission barrier that eventually leads to high fission cross sections [26]. Fission fragment mass distribution (FFMD) is one of the important yet complex postscission observables. Investigation of FFMD as a function of excitation energy ( $E^*$ ) of the composite system is of great interest as it influences the mass distribution. Maximum contribution of the asymmetric component in the distribution for sub-lead isotopes at low  $E^*$  has been studied; even for some isotopes, single-mode fission (i.e., asymmetric mode) has been reported [27]. However, as the  $E^*$  increases, the shell effects start washing out, and symmetric component contribution starts dominating.  $E^*$  is also related to the width of FFMD, and the rise in its value with increasing  $E^*$  of fissioning nuclei shows an increase in the spread of fission-fragment masses. Dispersion parameters have been deduced for a number of target-projectile combinations, such as  $^{19}\text{F} + ^{169}\text{Tm}$  [28],  $^{11}\text{B} + ^{181}\text{Ta}$  [29],  $^{11}\text{B} + ^{232}\text{Th}$  [30],  $^{16}\text{O} + ^{181}\text{Ta}$  [31],  $^{11}\text{B} + ^{209}\text{Bi}$  and  $^{181}\text{Ta}$  [32],  $^{12}\text{C} + ^{169}\text{Tm}$  [33],  $^{14}\text{N} + ^{181}\text{Ta}$  [34], and their mass variance behavior with changing  $E^*$ , mass asymmetry, and angular momentum also have been reported by some of the authors. Further, study of fission observables in  $^{12}\text{C} + ^{181}\text{Ta}$  system have been reported at energies  $>13$  MeV/nucleon [35], 3.65 A GeV [36], and 47 MeV/nucleon [37].

It may be noted that Crippa *et al.* [38], and Babu *et al.* [39] studied the  $^{12}\text{C} + ^{181}\text{Ta}$  system at relatively low energies, 4.5–8.2 and 5–6.5 MeV/nucleon, respectively. However, it has been mentioned in Ref. [38] that abundance information for some evaporation residues (ERs) is of poor quality, and relative values have been used for the calculation of CF and ICF cross sections. Also, instead of individual ER excitation function analysis, the CF cross section has been compared with the predictions by Bass and Thomas [40] in Ref. [38]. Fission cross sections also have been calculated, but at higher energies,  $E_{\text{lab}} \geq 72.6$  MeV. Whereas in the present study,

significant fission cross sections have been observed even at energies below this. The authors in Ref. [39] were restricted only to residue measurement, with no mention of fission data, and used one level density parameter,  $A/8$  MeV $^{-1}$ , in PACE2 code while comparing the measurements.

On the other hand, two theoretical model codes, PACE4 [41] and EMPIRE3.2.2 [42], have been incorporated in the present study for a better understanding of the reaction mechanism. Moreover, ICF fractions have been estimated from our measured data, and those reported in Ref. [39] considering PACE4 as a reference. Hence, the present study will give a comprehensive overview of the possible mechanisms involved at chosen energy range for the  $^{12}\text{C} + ^{181}\text{Ta}$  system.

The experimental details and brief of theoretical calculations are presented in Secs. II and III, respectively. Section IV discusses the results of the present study, and Sec. V concludes the report.

## II. EXPERIMENTAL DETAILS

The experiment was performed at the 14UD BARC-TIFR Pelletron Accelerator facility, Mumbai, India, using  $^{12}\text{C}$ -ion beam having energy within 52–73 MeV in the laboratory frame of reference. Self-supporting pure (99.99%) natural tantalum ( $^{181}\text{Ta}$ ) targets having a thickness within 1.4–1.8 mg/cm $^2$  were prepared by the rolling method. A total of four stacks, each of which contains two sets of Ta-Al foils, were irradiated by  $^{12}\text{C}$ -ion beam. The arrangement of target and catcher in stacks is similar to that shown in Ref. [43]. Aluminum foil was placed behind each Ta foil for energy degradation and catching the ERs in the forward beam direction. Measurements have been done using the stacked-foil technique followed by off-line  $\gamma$  spectrometry, as popularly used in literature too [44–47]. The degradation of energy in each foil was estimated by SRIM (stopping and range of ions in matter) code [48]. The estimate of energy at the center of a target is the average of the incident and outgoing beam energy. The projectile energies at each Ta target are  $72.7 \pm 0.9$ ,  $68.1 \pm 0.9$ ,  $63.3 \pm 1.0$ ,  $62.2 \pm 0.9$ ,  $57.8 \pm 1.0$ ,  $57.2 \pm 1.0$ , and  $52.0 \pm 0.8$  MeV. A constant beam current of  $\approx 10$  pA was maintained throughout the experiment, and an average charge of  $\approx 733$   $\mu\text{C}$  was collected by the Faraday cup installed behind the target stack.

After the end of the bombardment, each target catcher (Ta-Al) set was assayed with the help of  $\gamma$ -ray spectroscopy using a large volume high purity germanium detector coupled with a PC-based multichannel analyzer and GENIE-2K software. Residues were identified through their characteristic  $\gamma$  rays and decay profile. The detector having energy resolution 2.0 keV at 1332 keV  $\gamma$  ray of  $^{60}\text{Co}$  was precalibrated by using the standard sources,  $^{152}\text{Eu}$  (13.517 y),  $^{137}\text{Cs}$  (30.08 y), and  $^{60}\text{Co}$  (5.27 y) of known activity. The spectroscopic data of the ERs and fission fragments are given in Table I and Table II, respectively.

The cross section of  $i^{\text{th}}$  residue,  $\sigma_i(E)$ , at an incident energy,  $E$  is calculated from the below-mentioned equation:

$$\sigma_i(E) = \frac{\lambda_i N_i(t) e^{\lambda_i t_w}}{\varepsilon_\gamma I_\gamma A_{t,g} \phi (1 - e^{-\lambda_i t_r})(1 - e^{-\lambda_i t_c})}, \quad (1)$$

TABLE I. Spectroscopic data [57,58] of the radionuclides formed through CF/ICF processes in  $^{12}\text{C} + ^{181}\text{Ta}$  system.

Nuclides	$J^\pi$	Decay mode (%)	Half-life	$E_\gamma$ (keV)	$I_\gamma$ (%)
$^{190g}\text{Au}$	$1^-$	$\epsilon^a + \beta^+$ (100)	42.8 min	295.82	90.0
				301.82	30.0
				597.68	12.0
				1057.7	4.4
				1441.3	5.0
$^{189m}\text{Au}$	$11/2^-$	$\epsilon + \beta^+$ (100)	4.59 min	166.4	59.0
$^{188}\text{Au}$	$1^-$	$\epsilon + \beta^+$ (100)	8.84 min	265.63	36.5 <sup>b</sup>
				340.04	8.7 <sup>b</sup>
$^{189}\text{Pt}$	$3/2^-$	$\epsilon + \beta^+$ (100)	10.87 h	94.34	6.5
				113.82	2.5
				223.34	1.3
				243.5	5.9
				317.65	2.8
				544.91	4.9
$^{187g}\text{Ir}$	$3/2^+$	$\epsilon + \beta^+$ (100)	10.5 h	568.85	6.0
				721.38	7.9
				912.86	4.3
$^{186g}\text{Ir}$	$5^+$	$\epsilon + \beta^+$ (100)	16.64 h	434.84	33.9
				773.28	8.9

<sup>a</sup>Electron capture.

<sup>b</sup>Derived from relative intensity information given in Ref. [58].

where,  $\lambda_i$  and  $N_i(t)$  are decay constant and area count under the photo peak, respectively.  $\epsilon_\gamma$  and  $I_\gamma$  are the geometry-dependent detector efficiency and branching intensity of the characteristic  $\gamma$  ray of the residue, respectively.  $A_{t,g}$  is the areal density of the target nuclei and  $\phi$  is the incident beam flux.  $t_r$ ,  $t_c$ , and  $t_w$  are the irradiation time, counting time, and waiting time between EOB and the measurement, respectively. The factors that are responsible for the uncertainty in cross section measurement and energy are:

- (1) Uncertainty in the efficiency calibration of the detector ( $\leq 2\%$ ).
- (2) Uncertainty in the measurement of target thickness (2%).
- (3) Uncertainty in the beam flux due to beam current fluctuations (6–7%).
- (4) Statistical error in the background-subtracted peak area count.
- (5) Error in the estimation of beam energy due to energy degradation while passing through successive target-catcher foils. However, energy straggling was considered to be less.

The total uncertainty associated with the cross section measurement was estimated by considering all the factors mentioned above.

### III. THEORETICAL CALCULATIONS

The theoretical estimations of residual cross sections have been done for  $^{12}\text{C} + ^{181}\text{Ta}$  reaction using nuclear reaction model codes, PACE4 [41] and EMPIRE3.2.2 [42] within

50–80 MeV incident energy range. Brief details regarding the used statistical codes and the input parameters used for the calculations are given below.

In PACE4, the decay of excited CN is traced using the Monte Carlo method. Conservation of energy and angular momentum is considered at each stage of particle evaporation. The code is based on Hauser-Feshbach (HF) formalism, which follows the angular momentum coupling at each stage of de-excitation of an excited nucleus. For heavy projectiles, fusion cross section and initial spin distribution are calculated by the Bass model [49]. However, it can not determine heavy-ion fusion near and below the barrier and reaction induced by very heavy beams. Fission is considered as a decay mode and is calculated by using a modified rotating liquid drop fission barrier given by Sierk [50]. During deexcitation of the excited CN, light particles such as  $n$ ,  $p$ , and  $\alpha$  are emitted, for which the transmission coefficients are obtained by using the optical model calculations, whose parameters are taken from Ref. [51]. In the expression  $a = A/K$ ,  $a$  defines the level density parameter,  $A$  is the mass number of CN, and  $K$  is a free parameter whose value may be varied. In the present study, we have used  $K = 9$  and  $10$ . The value of  $a$  ratio,  $a_f/a_n$  (where,  $a_f$  and  $a_n$  are the level density parameters for fission and neutron emissions), is taken as unity. Quantum mechanical transmission probability below the barrier is taken into account. PACE4 does not account for direct (DIR) processes and PEQ emissions, and one can estimate the total production cross section of a particular residue.

EMPIRE3.2.2 considers all the three major nuclear reaction formalisms – DIR, PEQ, and EQ. The HF model is used for the compound reaction process. For fission calculations, the optical model is used. Coupled-channels calculation (CCFUS) is used for heavy-ion fusion cross section [52]. Nuclear masses, optical model parameters, ground-state deformations, discrete levels and decay schemes, level densities, fission barriers, and  $\gamma$ -ray strength functions are internally provided by input library RIPL-3 [53]. Some more details on EMPIRE3.2.2 are available in literature [54,55]. In our calculation, the phenomenological PEQ model (exciton model) with a mean-free path parameter of 1.5 is used for the PEQ emission process. EMPIRE3.2.2 code facilitates several nuclear level density models, out of which we have used Gilbert-Cameron model (GC) [56], in which the collective (rotational/vibrational) effect of nuclei on nuclear level density is considered.

### IV. RESULTS AND DISCUSSION

The  $\gamma$ -ray spectra collected from each Ta-Al set after the EOB have been analyzed to identify the residual radionuclides produced in the  $^{12}\text{C} + ^{181}\text{Ta}$  reaction at different incident energies. It ensured the production of  $^{190g}\text{Au}$ ,  $^{189g}\text{Au}$ ,  $^{189m}\text{Au}$ ,  $^{188}\text{Au}$ ,  $^{189}\text{Pt}$ ,  $^{187g}\text{Ir}$ , and  $^{186g}\text{Ir}$  in the target matrix. Additionally, several other residues with charge and atomic mass values around half of the aforementioned residues have been identified. This indicates the occurrence of fission of CN formed through CF and/or ICF processes, which led to the production of  $^{71m}\text{Zn}$ ,  $^{73}\text{Se}$ ,  $^{74m}\text{Br}$ ,  $^{83}\text{Br}$ ,  $^{85m}\text{Y}$ ,  $^{86}\text{Y}$ ,  $^{93m}\text{Mo}$ ,  $^{104}\text{Ag}$ ,  $^{107}\text{Rh}$ ,  $^{122}\text{Xe}$ ,  $^{132}\text{I}$ , and  $^{135}\text{Ce}$  fission fragments. A  $\gamma$ -ray

TABLE II. Spectroscopic data [57,58] of the fission fragments formed in  $^{12}\text{C} + ^{181}\text{Ta}$  system.

Nuclides	$J^\pi$	Decay mode (%)	Half-life	$E_\gamma$ (keV)	$I_\gamma$ (%)
$^{71m}\text{Zn}$	$9/2^+$	$\beta^-$ (100)	3.96 h	1107.5	2.0
$^{73}\text{Se}$	$9/2^+$	$\epsilon + \beta^+$ (100)	7.15 h	67.03	78.0
$^{74m}\text{Br}$	$4^+$	$\epsilon + \beta^+$ (100)	46 min	615.17	6.7
$^{83}\text{Br}$	$3/2^-$	$\beta^-$ (100)	2.4 h	529.63	1.2
$^{85m}\text{Y}$	$9/2^+$	$\epsilon + \beta^+$ (100)	4.86 h	767.4	3.6
$^{86}\text{Y}$	$4^-$	$\epsilon + \beta^+$ (100)	14.74 h	645.9	9.2
$^{93m}\text{Mo}$	$21/2^+$	$\text{IT}^a$ (99.88) $\epsilon + \beta^+$ (0.12)	6.85 h	1477.13	99.1
$^{104}\text{Ag}$	$5^+$	$\epsilon + \beta^+$ (100)	69.2 min	362.3	1.3
$^{107}\text{Rh}$	$7/2^+$	$\beta^-$ (100)	21.7 min	670.05	2.22
$^{122}\text{Xe}$	$0^+$	$\epsilon$ (100)	20.1 h	350.06	7.8
$^{132}\text{I}$	$4^+$	$\beta^-$ (100)	2.29 h	812.0	5.5
$^{135}\text{Ce}$	$1/2^+$	$\epsilon + \beta^+$ (100)	17.7 h	828.38	5.14

<sup>a</sup>Isomeric transition.

spectrum of 68.1 MeV  $^{12}\text{C}$  irradiated  $^{181}\text{Ta}$ , collected after 26.3 min of the EOB is shown in Fig. 1 and the characteristic  $\gamma$  peaks corresponding to each residue have been marked. The spectrum also includes  $\gamma$  peaks associated with  $^{34m}\text{Cl}$  and  $^{24}\text{Na}$  residues, which might have been produced due to the interaction of  $^{12}\text{C}$  beam with the backing material,  $^{27}\text{Al}$ , during irradiation. It is worth mentioning that the marking of extra peaks belonging to premarked residues have been

omitted to avoid overcrowding the spectrum. The confirmation of residues has also been obtained from the estimation of their half-lives, a representative decay profile for 721.38 keV  $\gamma$  line of  $^{189}\text{Pt}$  at 63.3 MeV incident energy and its half-life estimate is shown in the inset of Fig. 1. The calculated half-life ( $11.0 \pm 0.1$  h) is close to the literature value (10.87 h) [57,58]. The background-subtracted and dead-time corrected peak area of all the characteristic  $\gamma$  rays of each residue has been

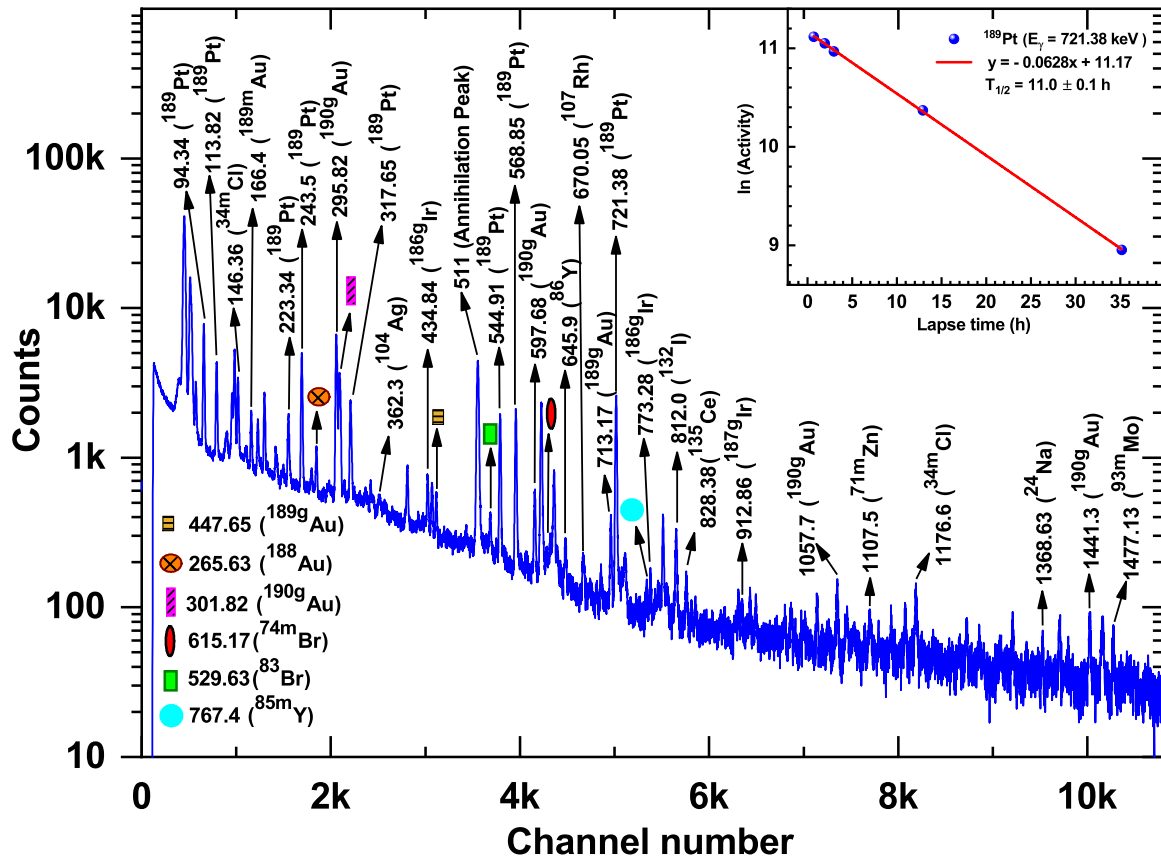


FIG. 1. A typical  $\gamma$ -ray spectrum of  $^{181}\text{Ta}$  irradiated by  $E_{\text{lab}} = 68.1$  MeV  $^{12}\text{C}$  beam, collected after 26.3 min of EOB. The energy of  $\gamma$ -ray peaks are in keV.



TABLE III. Cross section (mb) of evaporation residues and fission fragments at various incident energies.

Residues( $\downarrow$ )	Cross section (mb)						
	$E_{\text{lab}}$ (MeV)( $\rightarrow$ )	$E_{\text{c.m.}}$ (MeV)( $\rightarrow$ )					
$E_{\text{lab}}$ (MeV)( $\rightarrow$ )	$72.7 \pm 0.9$	$68.1 \pm 0.9$	$63.3 \pm 1.0$	$62.2 \pm 0.9$	$57.8 \pm 1.0$	$57.2 \pm 1.0$	$52.0 \pm 0.8$
$E_{\text{c.m.}}$ (MeV)( $\rightarrow$ )	$68.2 \pm 0.8$	$63.9 \pm 0.8$	$59.4 \pm 0.9$	$58.3 \pm 0.8$	$54.2 \pm 0.9$	$53.6 \pm 0.9$	$48.8 \pm 0.8$
$^{71m}\text{Zn}$	—	$26.4 \pm 5.4$	$0.5 \pm 0.1$	—	—	—	—
$^{73}\text{Se}$	—	—	—	—	—	—	$0.5 \pm 0.1$
$^{74m}\text{Br}$	—	$3.7 \pm 1.0$	$7.7 \pm 2.0$	$11.8 \pm 2.0$	$17.0 \pm 2.8$	$7.1 \pm 1.6$	—
$^{83}\text{Br}$	$46.7 \pm 11.1$	$45.4 \pm 9.6$	$79.6 \pm 15.0$	$92.9 \pm 15.3$	$20.2 \pm 6.2$	—	—
$^{85m}\text{Y}$	$25.7 \pm 4.4$	$10.5 \pm 2.6$	$14.3 \pm 3.5$	—	—	—	—
$^{86}\text{Y}$	$31.8 \pm 5.0$	$28.5 \pm 4.5$	$42.0 \pm 6.0$	$17.2 \pm 4.2$	$7.1 \pm 1.9$	—	—
$^{93m}\text{Mo}$	$1.2 \pm 0.2$	$1.0 \pm 0.2$	$1.7 \pm 0.3$	—	—	—	—
$^{104}\text{Ag}$	—	$40.7 \pm 7.9$	$107.2 \pm 18.6$	$101.3 \pm 15.0$	$90.9 \pm 18.3$	$72.9 \pm 12.7$	—
$^{107}\text{Rh}$	$215.3 \pm 27.5$	$179.2 \pm 32.9$	$158.4 \pm 27.7$	—	—	—	—
$^{122}\text{Xe}$	$29.6 \pm 5.7$	$18.5 \pm 4.2$	$26.8 \pm 6.0$	$14.2 \pm 3.9$	—	—	—
$^{132}\text{I}$	$33.6 \pm 4.5$	$28.5 \pm 3.8$	$37.5 \pm 5.3$	$32.4 \pm 4.7$	$13.8 \pm 2.8$	—	—
$^{135}\text{Ce}$	$38.1 \pm 6.7$	$34.3 \pm 6.2$	$56.3 \pm 9.2$	$27.6 \pm 8.0$	—	—	—
$^{190g}\text{Au}$	$10.4 \pm 1.8$	$19.0 \pm 3.2$	$56.1 \pm 8.8$	$67.3 \pm 7.7$	$44.0 \pm 8.5$	$28.5 \pm 4.8$	$0.9 \pm 0.2$
$^{189g}\text{Au}$	$375.4 \pm 79.8^a$	$264.4 \pm 79.0^a$	$324.6 \pm 49.2^a$	$172.8 \pm 35.2^a$	$83.8 \pm 10.1^a$	$13.1 \pm 2.8^a$	—
$^{189m}\text{Au}$	$201.5 \pm 20.3$	$230.5 \pm 26.4$	$91.7 \pm 4.3$	$55.0 \pm 5.8$	—	—	—
$^{188}\text{Au}$	$257.7 \pm 25.5$	$29.7 \pm 3.6$	—	—	—	—	—
$^{189}\text{Pt}$	$595.6 \pm 63.1$	$508.6 \pm 56.0$	$431.9 \pm 47.2$	$236.1 \pm 30.9$	$87.7 \pm 10.6$	$13.7 \pm 2.9$	—
$^{187g}\text{Ir}$	$19.7 \pm 4.5$	$20.1 \pm 4.4$	$13.6 \pm 4.2$	$11.4 \pm 4.3$	—	—	—
$^{186g}\text{Ir}$	$41.1 \pm 5.5$	$18.5 \pm 2.6$	$18.6 \pm 2.5$	$3.9 \pm 1.1$	$1.6 \pm 0.4$	—	—

<sup>a</sup>Derived.

analyzed to measure the activity and hence, the residual cross section ( $\sigma$ ) by using Eq. (1).

### A. Residual cross section

The cross sections calculated for the residues populated through CF and ICF at various energies are shown in Table III. The experimentally measured excitation functions for ERs are compared with the experimental data reported by Crippa *et al.* [38] and Babu *et al.* [39] for the same system,  $^{12}\text{C} + ^{181}\text{Ta}$ , and the theoretically computed excitation functions using the nuclear reaction model codes PACE4 [41] and EMPIRE3.2.2 [42] as shown in Figs. 2 and 3. Theoretical calculations are shown by curves, while experimentally measured cross sections are shown by symbols with the error bar, except for the data reported by Ref. [38].

#### 1. $xn$ channel

Three radionuclides,  $^{190g}, ^{189(g+m)}, ^{188}\text{Au}$  have been observed in the  $\gamma$ -ray spectra through the evaporation of neutrons from CN. Figure 2(a) shows the excitation function of  $^{190g}\text{Au}$ , produced through  $^{181}\text{Ta}(^{12}\text{C}, 3n)$  reaction. Data reported by Refs. [38] and [39] are grossly satisfying the measured excitation function. It is also observed that EMPIRE3.2.2 with level density GC is satisfactorily reproducing the data only at lower-energy point, 52.0 MeV, while at higher-energy region EMPIRE is overpredicting the data. The effect of different models in estimating fusion below the barrier energy region by PACE4 and EMPIRE can be observed in Fig. 2(a). The one-dimensional barrier penetration model used by PACE4 predicted quite low cross sections below the barrier. On the other hand, incorporation of coupled-channels calculation by EMPIRE estimates adequate cross sections in the lower-

energy region. However, PACE4 is reproducing the measured cross sections well at energies  $>52.0$  MeV, except for the higher-energy point, 72.7 MeV. Since PACE4 computation is based only on the HF formalism, a compound nuclear model, it is evident that no PEQ emission occurs in this case. Hence, the formation of  $^{190g}\text{Au}$  ( $3n$  channel) can be regarded through an equilibrium mechanism.

Excitation function of  $^{189(g+m)}\text{Au}$ , produced through  $^{181}\text{Ta}(^{12}\text{C}, 4n)$  reaction, is shown in Fig. 2(b). Since relative intensity information for  $^{189g}\text{Au}$  is available in literature instead of absolute intensity, the cross sections for this radionuclide have been calculated through the production of  $^{189}\text{Pt}$ . As the half-life of  $^{189g}\text{Au}$  (28.7 min) is short compared to the large half-life of  $^{189}\text{Pt}$  (10.87 h), one can expect that the production observed in  $^{189}\text{Pt}$  is almost coming from the decay of its parent nuclei,  $^{189}\text{Au}$ . Moreover, theoretical models predict very less cross section for  $^{189}\text{Pt}$ , as they only give independent cross section estimates for the residues. Hence, we have used the relation given below to calculate the cross sections for  $^{189(g+m)}\text{Au}$  by assuming negligible independent cross section for  $^{189}\text{Pt}$  [59],

$$\sigma_{^{189}\text{Pt}}^{(C)} = \sigma_{^{189}\text{Pt}}^{(I)} + 1.046\sigma_{^{189g}\text{Au}} + 1.007\sigma_{^{189m}\text{Au}}. \quad (2)$$

An experimentally measured cross section for  $^{189m}\text{Au}$  is used to calculate the cross section for  $^{189g}\text{Au}$ . From Fig. 2(b) it can be observed that our measured excitation function is in good agreement with that of Babu *et al.* [39]. The cross sections for  $^{189g}\text{Au}$  are reported in (mb), whereas those for  $^{189m}\text{Au}$  are reported in arbitrary unit (a.u.) in Ref. [38]. Hence, that data could not be compared with the measured cross sections of  $^{189}\text{Au}$ . Theoretical estimates from PACE4 and EMPIRE are following the trend similar to the measured

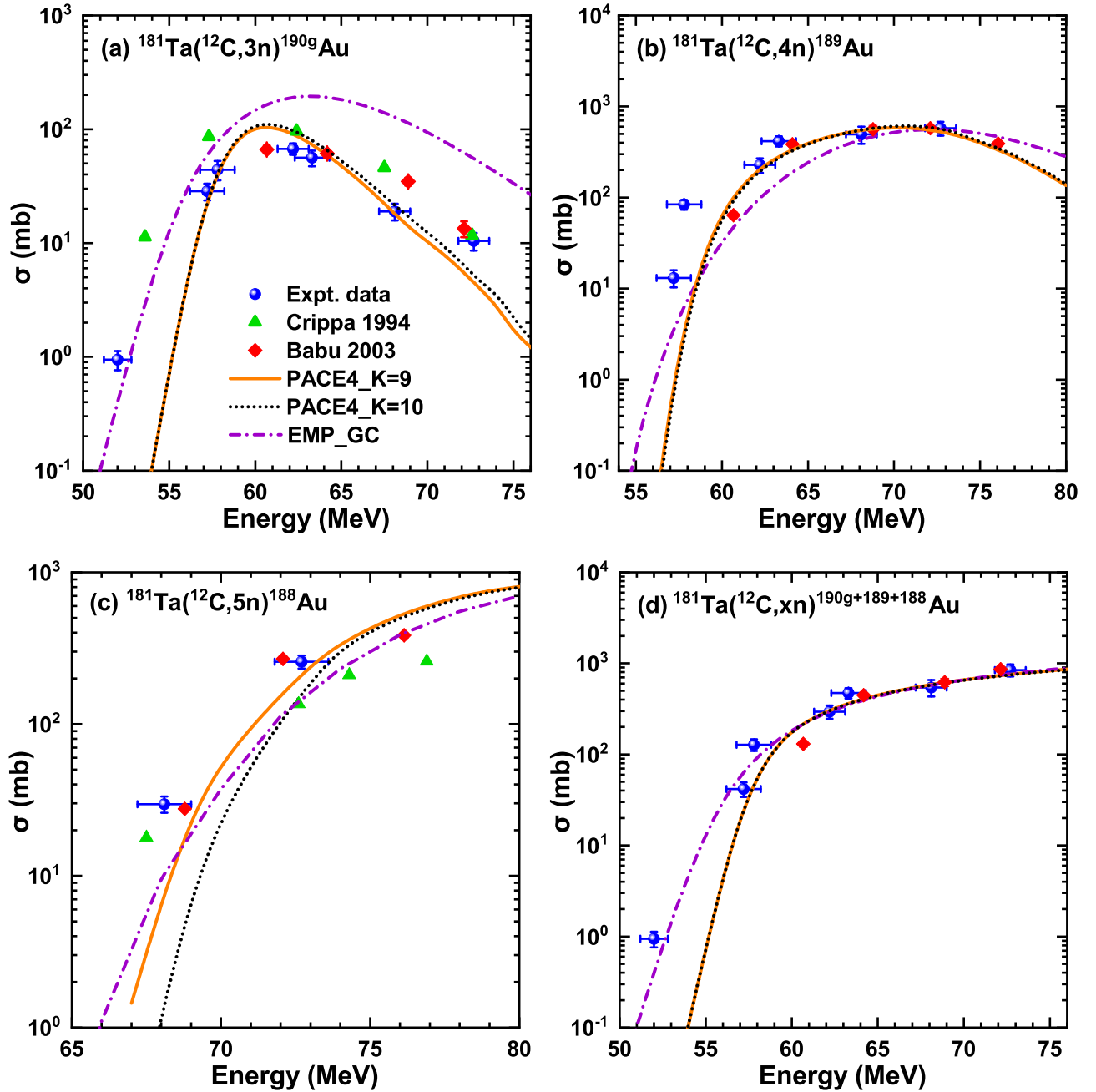


FIG. 2. Comparison of measured excitation function of (a)  $^{190g}\text{Au}$ , (b)  $^{189}\text{Au}$ , (c)  $^{188}\text{Au}$ , and (d)  $^{190g+189+188}\text{Au}$  with theoretical predictions from PACE4 and EMPIRE3.2.2 (denoted by EMP), and the data reported by Crippa 1994 [38] and Babu 2003 [39].

excitation function. However, PACE4 with  $K = 9$  is reproducing the data best. It also ensures the absence of the PEQ process in the  $xn$  channel.

The half-life of  $^{188}\text{Pt}$  (10.2 d) is very large as compared to  $^{188}\text{Au}$  (8.84 min). Similar to the case of  $^{189}\text{Au}$ , it is expected that the decay of  $^{188}\text{Au}$  would produce a considerable amount of  $^{188}\text{Pt}$ . However, we have not identified any  $\gamma$  peak for  $^{188}\text{Pt}$  in the present study. Therefore, the direct cross section estimation method for  $^{188}\text{Au}$  via identification of its  $\gamma$  peaks from the spectra has been adopted. Figure 2(c) represents the comparison of measured and theoretical excitation func-

tions of  $^{188}\text{Au}$ . Experimental data is in better agreement with PACE4 with  $K = 9$ , but EMPIRE underpredicts the measured data. The measured excitation function is also compared with the data reported in Refs. [38,39]. It is observed that cross sections reported by Crippa *et al.* [38] are much lower than the present measured data. The observed divergence might be due to the use of relative intensity for the  $\gamma$  lines of  $^{188}\text{Au}$  instead of absolute intensity in the cross section calculations reported in Ref. [38]. The influence of the choice of characteristic  $\gamma$ -ray intensity on the cross section can be understood based on Eq. (1). As the relative intensities have

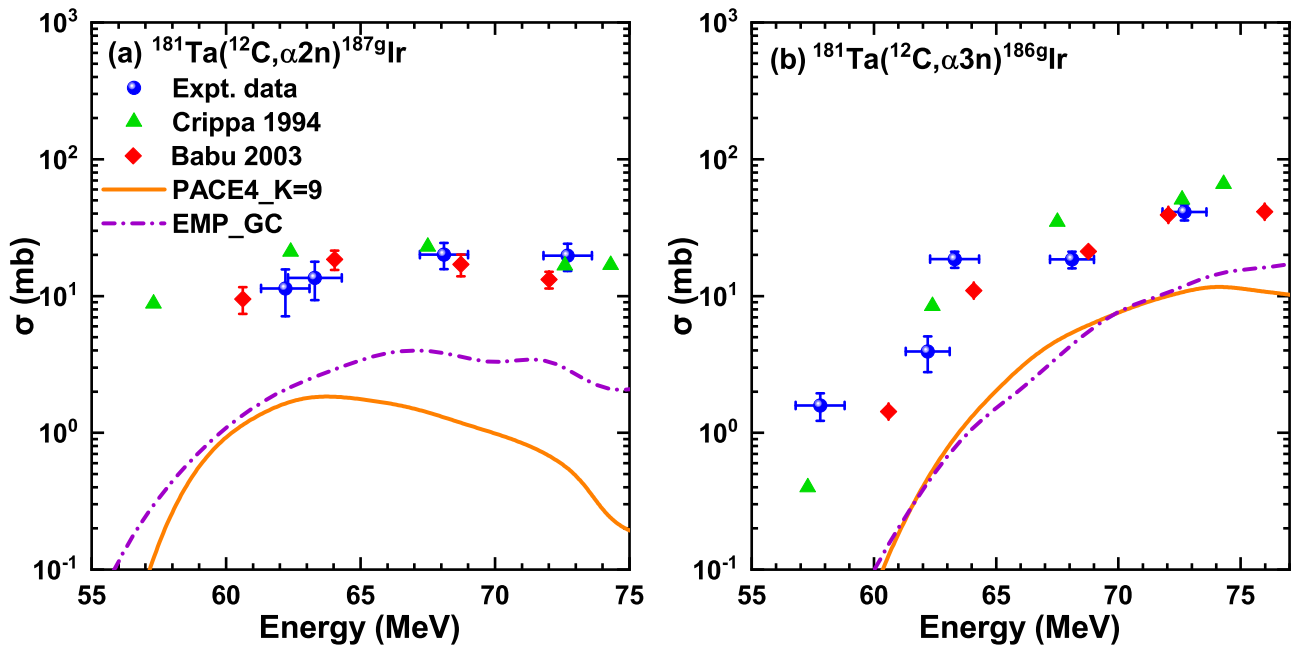


FIG. 3. Same as that of Fig. 2 for (a)  $^{187g}\text{Ir}$  and (b)  $^{186g}\text{Ir}$ .

higher values as compared to the absolute intensities used in the present calculation, the lower cross sections can be seen in Ref. [38]. On the other hand, cross sections reported by Ref. [39] are in good agreement with the measured excitation function within the uncertainty limit.

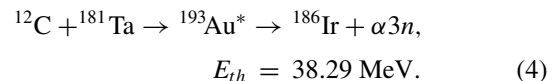
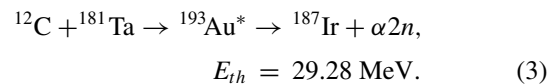
The sum of experimentally measured excitation functions of all the  $xn$  reaction channel residues is compared with the sum of theoretical excitation functions, as shown in Fig. 2(d). It can be observed that EMPIRE with GC satisfactorily reproduces our measurements. PACE4 predictions are also in good agreement with our measurements except below the Coulomb barrier energies ( $E_{\text{lab}} < 57.2$  MeV). Hence, we can say that below the barrier, PACE4 is unable to reproduce the data. No evidence of PEQ emission is observed in the  $xn$  reaction channel. It can be concluded that all three radionuclides  $^{190g}\text{Au}$ ,  $^{189(g+m)}\text{Au}$ , and  $^{188}\text{Au}$  produced through  $3n$ ,  $4n$ , and  $5n$  channel, respectively, are formed through the equilibrium process. The sum of  $xn$  reaction channel cross sections reported by Ref. [39] also can be seen as consistent with our data. So far, we have observed that PACE4 with  $K = 9$  and EMPIRE with level density GC are reproducing our data well. Therefore, the measured excitation functions of the remaining residues produced through the  $\alpha xn$  channel have been compared with them.

## 2. $\alpha xn$ channel

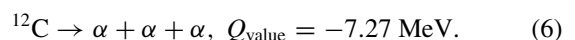
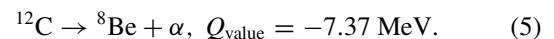
Figure 3(a) represents the excitation function for  $^{187g}\text{Ir}$  radionuclide. Our measurements are consistent with the observations reported by Refs. [38] and [39] for this radionuclide. However, a significant enhancement in the measured cross sections is observed after comparing it with the theoretical estimations given by PACE4 and EMPIRE. Similar behavior is encountered in the case of  $^{186g}\text{Ir}$ , which is formed through  $^{181}\text{Ta}(^{12}\text{C}, \alpha 3n)$  reaction. From Fig. 3(b), we can observe the

enhancement in the experimental data as compared to the theoretical predictions. The reason behind this observation may be the breakup of the projectile ( $^{12}\text{C}$ ) into fragments before fusing to the target nuclei. Hence, it is assumed that the observed enhanced experimental data over the theoretical predictions might be due to the contribution coming from ICF along with the CF process. Crippa *et al.* [38] and Babu *et al.* [39] also reported the presence of ICF in the  $\alpha xn$  channel. Thus, we can consider that both  $^{187g}\text{Ir}$  and  $^{186g}\text{Ir}$  might be produced by the following possible reaction channels:

(i) Complete fusion channel: The CF of  $^{12}\text{C}$  with  $^{181}\text{Ta}$  results in the formation of ( $^{193}\text{Au}^*$ ) CN, which leads to the production of  $^{187}\text{Ir}$  and  $^{186}\text{Ir}$  through  $\alpha 2n$  and  $\alpha 3n$  channels, respectively.



(ii) Incomplete fusion channel: As the projectile ( $^{12}\text{C}$ ) has an  $\alpha$ -cluster structure so in the presence of sufficient projectile energy and with the influence of nuclear force field, it can break up into fragments as shown below:



The possible breakups of the projectile mentioned above would lead to the formation of  $^{187g}\text{Ir}$  and  $^{186g}\text{Ir}$  when one of the fragments fuses with the target, and the other fragment moves in the forward direction as a spectator. For the ICF of  $^{12}\text{C}$ ,  $^8\text{Be}$  fragment might fuse with  $^{181}\text{Ta}$  target and lead to the

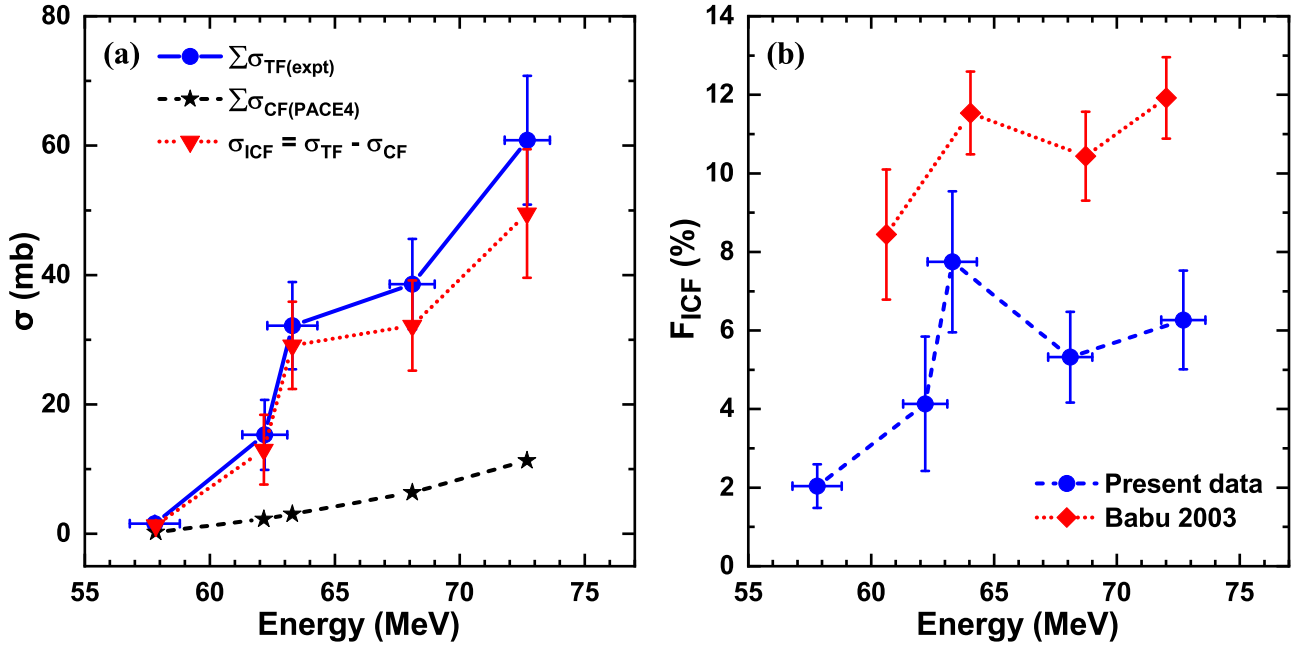
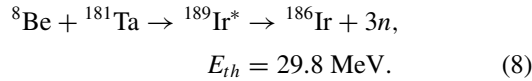
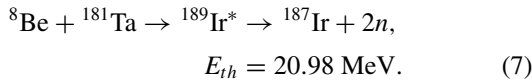


FIG. 4. (a) Variation of TF, CF, and ICF cross sections for  $\alpha$ -emitting channels and (b) Comparison of ICF fraction (%) deduced from present data and Babu 2003 [39].

formation of ( $^{189}\text{Ir}^*$ ) CN, which may produce  $^{187}\text{Ir}$  and  $^{186}\text{Ir}$  through  $2n$  and  $3n$  channel, respectively.



Sufficiently large cross sections than the theoretical estimates of PACE4 and EMPIRE in  $\alpha xn$  channels indicate the ICF mechanism in the present data. On the other hand, the fusion of  $\alpha$  fragment with  $^{181}\text{Ta}$  would not produce Ir radionuclides.

### B. ICF analysis

The ICF has been analysed for  $\alpha$ -emitting channels by using the data reduction method [10] with reference to the theoretical model calculations, PACE4 and/or EMPIRE. These models do not consider ICF in the calculations, which might be the reason for underprediction of cross section in the  $\alpha xn$  channels, whereas these models with same set of input parameters were observed satisfying the  $xn$  channel measurements. For  $xn$  channel, comparison of measured data with the theoretical models, as shown in Fig. 2, reveals that PACE4 with  $K = 9$  is more reliable than EMPIRE with GC. Hence, the total ICF cross section and strength of ICF is calculated in reference to PACE4 by using the relations:

$$\sum \sigma_{ICF} = \sum \sigma_{TF(expt)}^{187gIr+186gIr} - \sum \sigma_{CF(PACE4)}^{187Ir+186Ir} \quad (9)$$

$$F_{ICF}(\%) = \left( \sum \sigma_{ICF} / \sigma_{TF}^{theor} \right) \times 100\%. \quad (10)$$

Figure 4(a) represents the excitation function of total fusion (TF) cross section, which is the sum of experimentally measured cross sections of  $^{187g}\text{Ir}$  and  $^{186g}\text{Ir}$ , written in Eq. (9) as  $\sum \sigma_{TF(expt)}^{187gIr+186gIr}$ . It is compared with the sum of theoretical estimates given by PACE4 for  $^{187}\text{Ir}$  and  $^{186}\text{Ir}$ . Theoretically, only complete fusion is estimated; thus, it is total complete fusion cross section,  $\sum \sigma_{CF(PACE4)}^{187Ir+186Ir}$ . It is evident from Fig. 4(a) that TF is showing a significant enhancement than the CF. For estimating total ICF cross section,  $\sum \sigma_{ICF}$ , CF is subtracted from TF. In order to calculate the strength of ICF, the ratio of total ICF cross section (for  $\alpha xn$  channels) and total theoretical fusion cross section is taken, as mentioned in Eq. (10). Variation of  $F_{ICF}$  with the projectile energy can be seen in Fig. 4(b). A linear rise in the ICF strength is observed with the increasing incident energy except at 63.3 MeV, where an abrupt increase in  $F_{ICF}$  is observed. The  $F_{ICF}$  for the present data is compared with the  $F_{ICF}$  deduced from the data reported in Ref. [39] for the same system by incorporating the same theoretical model code (PACE4 with  $K = 9$ ). Although  $F_{ICF}$ , in this case, is also showing an increasing trend, it is relatively higher than the present data. This higher ICF strength fraction ( $\approx 3\text{--}5\%$ ) for Ref. [39] data might be due to the consideration of more number of  $\alpha$ -emitting channels (three  $\alpha xn$  and three  $2\alpha xn$  channels). While for our data, only two  $\alpha xn$  channels are considered for ICF strength fraction calculations. Considering two  $\alpha$ -emitting channels ( $\alpha 2n$  and  $\alpha 3n$ ) from present data as well as from Ref. [39],  $F_{ICF}$  per contributing channel has been calculated and found to be similar,  $\approx 2.0\text{--}3.8\%$  and  $\approx 2.0\text{--}3.2\%$ , respectively, for overlapping energy regions. It is worth mentioning that due to the limitations in the adopted technique, cross sections of stable residues and radionuclides having weak  $\gamma$  rays and very short half-lives are not measured. Thus, considering all these factors in mind, the ICF contri-



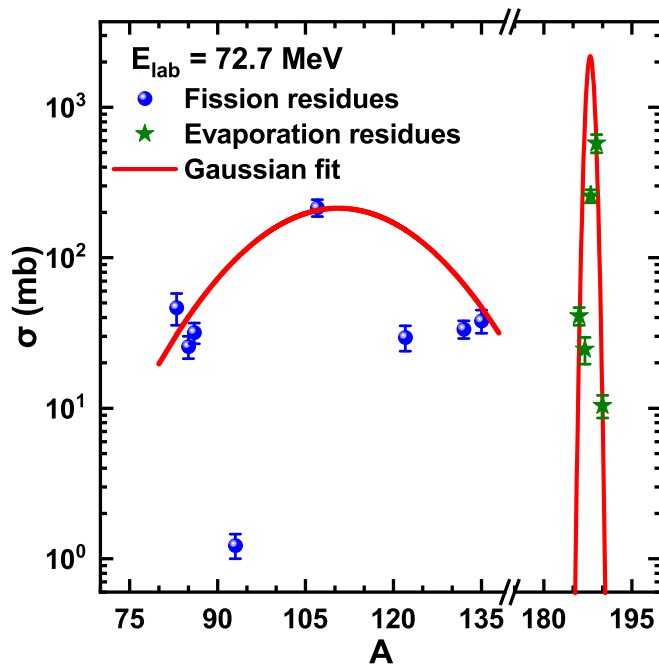


FIG. 5. Mass distribution of evaporation and fission residues produced through CF and/or ICF at  $E_{\text{lab}} = 72.7$  MeV. Solid lines show Gaussian fittings.

bution reported for the present data can be considered as the lowest limit of ICF contribution for the  $^{12}\text{C} + ^{181}\text{Ta}$  reaction in which up to 7.7% of  $F_{\text{ICF}}$  has been estimated.

### C. Mass distribution of fission fragments

Fission fragment mass distribution is one of the most interesting fission observables. It provides insight into the structure of potential energy surface (PES) and plays a significant role in identifying the different reaction mechanisms in heavy-ion-induced reactions. Several fissionlike events have been identified from the  $\gamma$  spectra recorded from each Ta-Al set. A total of 12 fission radionuclides within the mass range  $71 \leq A \leq 135$  have been identified in the present work, and the measured cross sections at different energies are represented in Table III. Theoretical model codes, PACE4 and EMPIRE, estimated very low fission cross sections in the considered energy range. It is worthy to note that even at the highest energy, 72.7 MeV, PACE4 estimated the fission cross section to be around 0.27 mb and EMPIRE estimated it to be zero. Contrary to these estimations, by summing the individual cross sections of fission fragments, the total fission cross sections have been measured in the order of several hundred or tens of mb, such as  $422.0 \pm 65.1$ ,  $416.6 \pm 78.4$ ,  $532.2 \pm 93.8$ ,  $297.4 \pm 53.2$ ,  $149.1 \pm 31.9$ ,  $79.9 \pm 14.4$ , and  $0.6 \pm 0.1$  mb at  $E_{\text{lab}} = 72.7, 68.1, 63.3, 62.2, 57.8, 57.2$ , and  $52.0$  MeV, respectively.

Figures 5 and 6 represent the experimentally measured individual cross sections of the fission fragments populated in the  $^{12}\text{C} + ^{181}\text{Ta}$  reaction as a function of mass number. Broad and symmetric mass distributions can be observed, at energies  $E_{\text{lab}} = 72.7, 68.1, 63.3, 62.2$ , and  $57.8$  MeV, which indicates

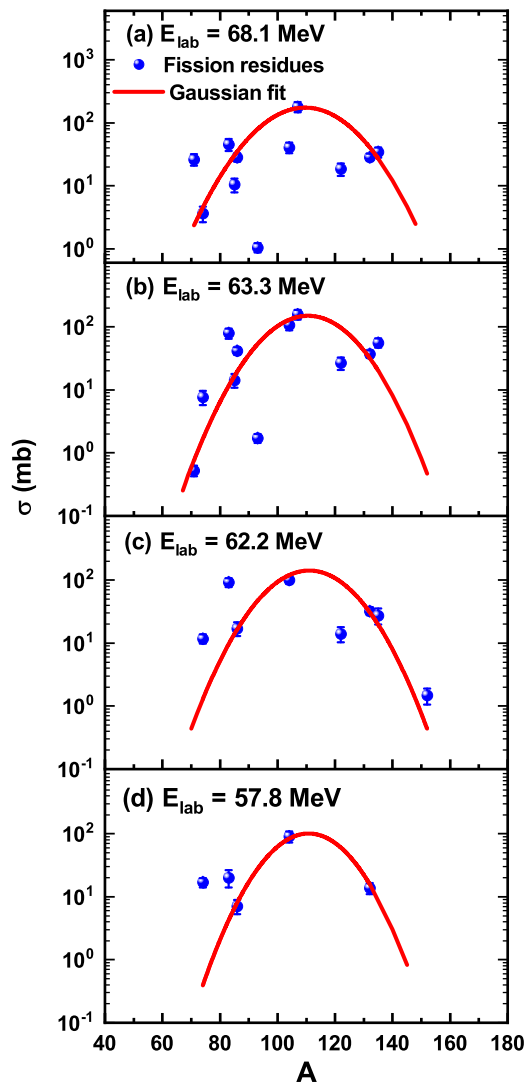


FIG. 6. FFMD at different incident energies. Gaussian fit is represented by solid line.

the formation of fission fragments from the compound nuclear mechanism, after fitting it with the Gaussian distribution. Hence, the independent yield is represented as:

$$Y(A) = ae^{-\frac{(A-M_{MP})^2}{2\sigma_M^2}}, \quad (11)$$

where,  $a$ ,  $M_{MP}$ , and  $\sigma_M$  are the peak amplitude, most probable mass (centroid), and width parameter, respectively, obtained from the Gaussian distribution. The energy points,  $E_{\text{lab}} > 57.2$  MeV, are above the Coulomb barrier, and maximum fission fragments have been identified in this energy region. On the other hand, only a few fission radionuclides, which are insufficient to fit with the Gaussian, were populated below the barrier. To explore the mass distribution of fission fragments below the barrier, longer time measurements are required. Using Gaussian fitting of the mass distribution in the present work, dispersion parameters ( $M_{MP}$ ,  $\sigma_M$ ) have been extracted as (110.6, 14.1) at  $E_{\text{lab}} = 72.7$  MeV, (109.6, 13.2) at  $E_{\text{lab}} = 68.1$  MeV, (110.6, 12.2) at  $E_{\text{lab}} = 63.3$  MeV, (111,

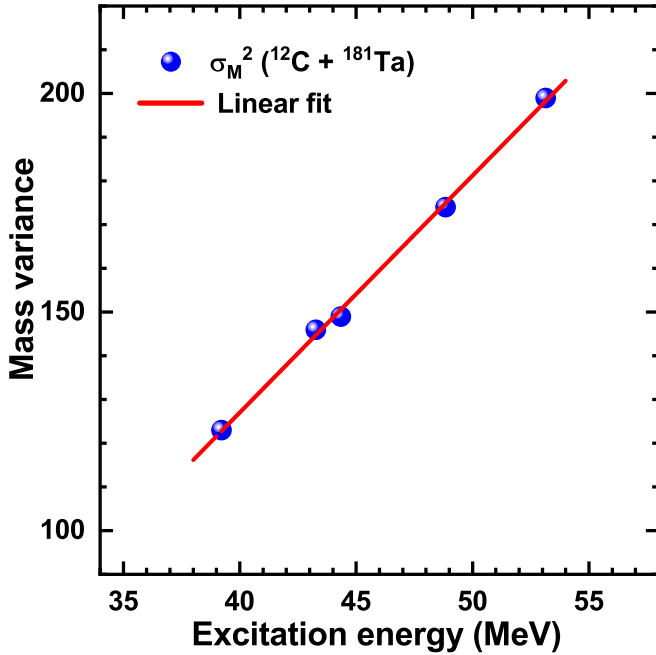


FIG. 7. Variation of mass variance of fission fragments' mass distribution with excitation energy for  $^{12}\text{C} + ^{181}\text{Ta}$  system. Linear fit is shown by red line.

12.1) at  $E_{\text{lab}} = 62.2$  MeV, and (110.8, 11.1) at  $E_{\text{lab}} = 57.8$  MeV.

The variance  $\sigma_M^2$  of the mass distribution has been found to be  $199 u^2$ ,  $174 u^2$ ,  $149 u^2$ ,  $146 u^2$ , and  $123 u^2$  at  $(E_{\text{lab}}, E^*) = (72.7, 53.1)$  MeV,  $(68.1, 48.8)$  MeV,  $(63.3, 44.3)$  MeV,  $(62.2, 43.3)$  MeV, and  $(57.8, 39.2)$  MeV, respectively. Figure 7 represents the linearly increasing trend of  $\sigma_M^2$  with increasing  $E^*$ , which indicates the broadening of mass distribution of fission fragments with increasing  $E^*$ . The smooth rise in  $\sigma_M^2$  with  $E^*$  is the property of fission through the complete fusion process. It can be explained on the basis of the liquid drop model, according to which temperature and angular momentum play an important role. Similar trend of rising variance is also reported in Refs. [28,33,34].

Furthermore, an attempt has been made to understand the role of entrance-channel mass asymmetry,  $\alpha = (M_T - M_P)/(M_T + M_P)$ , on the mass distribution of fission fragments. For this purpose, previously reported variance of FFMD for different target-projectile combinations,  $^{11}\text{B} + ^{232}\text{Th}$  [30] and  $^{16}\text{O} + ^{181}\text{Ta}$  [31], has been compared with the present system,  $^{12}\text{C} + ^{181}\text{Ta}$ , as a function of  $\alpha$ . This comparison has been made at  $E_{\text{lab}}/V_b$  value around 1.3 for the respective systems, where  $V_b$  represents Coulomb barrier in laboratory frame of reference. It can be clearly observed from Fig. 8 that mass variance increases with increasing mass asymmetry. Similar observations have been reported in Refs. [28,34] at fixed  $(E_{\text{lab}}/V_b)$  value. The study of  $\sigma_M^2$  over a wide range of  $\alpha$  values would help in understanding its dependence on  $\alpha$ .

Maximum input angular momentum ( $\ell_{\text{max}}$ ) also affects the distribution by varying the fission barrier ( $B_f$ ) [60,61]. Taking this under consideration, we have calculated  $\ell_{\text{max}}$  for each  $E^*$

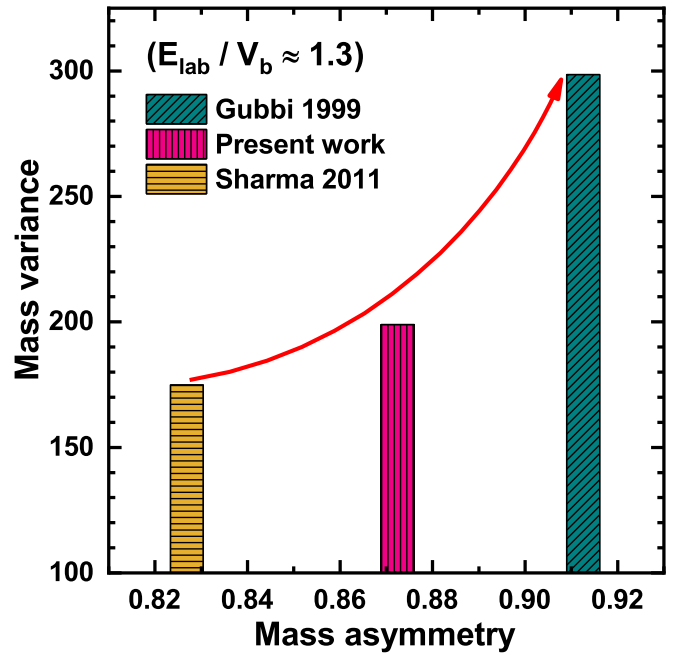


FIG. 8. Comparison of mass variance of present work with Gubbi 1999 [30] and Sharma 2011 [31] at normalized energy  $E_{\text{lab}}/V_b$ .

and found it to be  $6\hbar$ ,  $18\hbar$ ,  $20\hbar$ ,  $26\hbar$ , and  $32\hbar$  at 39.2 MeV, 43.3 MeV, 44.3 MeV, 48.8 MeV, and 53.1 MeV excitation energy, respectively. Calculations revealed its increasing trend with rising excitation energy. In addition, the cross sections of observed ERs forming through CF and/or ICF along with the fission fragments at  $E_{\text{lab}} = 72.7 \pm 0.9$  MeV have been plotted, as shown in Fig. 5. A broad and symmetric Gaussian peak represents the fissionlike events in the medium mass region,  $75 \leq A \leq 135$ . On the other hand, a narrow Gaussian in the heavy-mass region,  $180 \leq A \leq 195$ , indicates the formation of ERs through CF and/or ICF processes. Figure 5 separates the events coming from two different mechanisms in heavy-ion-induced reaction of the  $^{12}\text{C} + ^{181}\text{Ta}$  system.

## V. CONCLUSION

In conclusion, excitation functions for radionuclides produced through CF and ICF processes have been compared with theoretical model codes PACE4 and EMPIRE. Good agreement of PACE4 calculations, which is based on the Hauser-Feshbach formalism, in  $xn$  channel, implies the production of those radionuclides through the CF mechanism. Although reported data in Ref. [39] agree with the present data, variation up to a certain extent has been observed with data reported in Ref. [38]. Relatively large cross sections compared to theory in the  $\alpha xn$  channel indicate the presence of the ICF process. ICF fraction per observation channel in the present study and the one deduced from the reported data [39] is compared. Moreover, total fission cross sections have been estimated by adding the individual fission fragment cross sections measured at energies  $72.7 \pm 0.9$ ,  $68.1 \pm 0.9$ ,  $63.3 \pm 1.0$ ,  $62.2 \pm 0.9$ ,  $57.8 \pm 1.0$ ,  $57.2 \pm 1.0$ , and  $52.0 \pm 0.8$  MeV. The

FFMD at different  $E^*$  is broad and symmetric, indicating that the CN's deexcitation follows the fission process. The trend of mass variance with increasing  $E^*$  is found to be linearly increasing. The influence of entrance-channel parameters, especially mass asymmetry on mass variance has been observed for  $E_{\text{lab}}/V_b \approx 1.3$  value, and variance is found to be rising. A rise in the value of  $\ell_{\text{max}}$  with increasing  $E^*$  has been observed. This examination added an understanding regarding the observed increment in the fission cross section with increasing  $\ell_{\text{max}}$  as it tends to diminish the fission barrier gradually.

## ACKNOWLEDGMENTS

We sincerely thank the BARC-TIFR Pelletron team for their assistance during the experiment. We also appreciate our colleagues from Tasispec Lab, IIT Roorkee, for their help and passionate teamwork. Research Grant No. INT/RUS/RFBR/387 from DST(IN) and a student research fellowship from the UGC, Government of India, are gratefully acknowledged. The authors acknowledge the support of the Department of Atomic Energy, Government of India, under Project No. 12P-R&D-TFR-5.02-0300.

- [1] L. F. Canto, P. R. S. Gomes, R. Donangelo, J. Lubian, and M. S. Hussein, *Phys. Rep.* **596**, 1 (2015).
- [2] R. Prajapat and M. Maiti, *Phys. Rev. C* **101**, 024608 (2020).
- [3] R. Prajapat and M. Maiti, *Phys. Rev. C* **103**, 034620 (2021).
- [4] R. Prajapat and M. Maiti, *Phys. Rev. C* **101**, 064620 (2020).
- [5] A. Yadav, P. P. Singh, Mohd. Shuaib, V. R. Sharma, I. Bala, Unnati, S. Gupta, D. P. Singh, M. K. Sharma, R. Kumar, S. Murlithar, R. P. Singh, B. P. Singh, and R. Prasad, *Phys. Rev. C* **96**, 044614 (2017).
- [6] D. P. Singh, Unnati, P. P. Singh, A. Yadav, M. K. Sharma, B. P. Singh, K. S. Golda, R. Kumar, A. K. Sinha, and R. Prasad, *Phys. Rev. C* **81**, 054607 (2010).
- [7] P. P. Singh, A. Yadav, D. P. Singh, U. Gupta, M. K. Sharma, R. Kumar, D. Singh, R. P. Singh, S. Muralithar, M. A. Ansari, B. P. Singh, R. Prasad, and R. K. Bhowmik, *Phys. Rev. C* **80**, 064603 (2009).
- [8] I. Tserruya, V. Steiner, Z. Fraenkel, P. Jacobs, D. G. Kovar, W. Henning, M. F. Vineyard, and B. G. Glagola, *Phys. Rev. Lett.* **60**, 14 (1988).
- [9] U. Gupta, P. P. Singh, D. P. Singh, M. K. Sharma, A. Yadav, R. Kumar, B. P. Singh, and R. Prasad, *Nucl. Phys. A* **811**, 77 (2008).
- [10] D. Kumar, M. Maiti, and S. Lahiri, *Phys. Rev. C* **96**, 014617 (2017).
- [11] D. Kumar and M. Maiti, *Phys. Rev. C* **96**, 044624 (2017).
- [12] R. Kharab, R. Chahal, and R. Kumar, *Nucl. Phys. A* **946**, 1 (2016).
- [13] J. Rangel, M. R. Cortes, J. Lubian, and L. F. Canto, *Phys. Lett. B* **803**, 135337 (2020).
- [14] H. Kumar, S. A. Tali, M. A. Ansari, D. Singh, R. Ali, K. Kumar, N. P. M. Sathik, S. Parashari, A. Ali, R. Dubey *et al.*, *Nucl. Phys. A* **960**, 53 (2017).
- [15] S. Mukherjee, A. Sharma, S. Sodaye, A. Goswami, and B. S. Tomar, *Int. J. Mod. Phys. E* **15**, 237 (2006).
- [16] A. Yadav, V. R. Sharma, P. P. Singh, D. P. Singh, M. K. Sharma, U. Gupta, R. Kumar, B. P. Singh, R. Prasad, and R. K. Bhowmik, *Phys. Rev. C* **85**, 034614 (2012).
- [17] S. Chakrabarty, B. S. Tomar, A. Goswami, G. K. Gubbi, S. B. Manohar, A. Sharma, B. Bindukumar, and S. Mukherjee, *Nucl. Phys. A* **678**, 355 (2000).
- [18] S. Gupta, B. P. Singh, M. M. Musthafa, H. D. Bhardwaj, and R. Prasad, *Phys. Rev. C* **61**, 064613 (2000).
- [19] S. A. Tali, H. Kumar, M. A. Ansari, A. Ali, D. Singh, R. Ali, P. K. Giri, S. B. Linda, R. Kumar, S. Parashari, S. Muralithar, and R. P. Singh, *Phys. Rev. C* **100**, 024622 (2019).
- [20] Mohd. Shuaib, V. R. Sharma, A. Yadav, P. P. Singh, M. K. Sharma, D. P. Singh, R. Kumar, R. P. Singh, S. Muralithar, B. P. Singh, and R. Prasad, *Phys. Rev. C* **94**, 014613 (2016).
- [21] H. Kumar, S. A. Tali, M. A. Ansari, D. Singh, R. Ali, A. Ali, S. Parashari, P. K. Giri, S. B. Linda, R. Kumar, R. P. Singh, and S. Muralithar, *Phys. Rev. C* **99**, 034610 (2019).
- [22] D. Singh, P. K. Giri, A. Mahato, S. B. Linda, H. Kumar, M. A. Ansari, R. Ali, S. A. Tali, M. H. Rashid, R. Guin, and S. K. Das, *Nucl. Phys. A* **981**, 75 (2019).
- [23] S. A. Tali, H. Kumar, M. A. Ansari, A. Ali, D. Singh, R. Ali, P. K. Giri, S. B. Linda, S. Parashari, R. Kumar, R. P. Singh, and S. Muralithar, *Nucl. Phys. A* **970**, 208 (2018).
- [24] K. Nishio, H. Ikezoe, Y. Nagame, M. Asai, K. Tsukada, S. Mitsuoka, K. Tsuruta, K. Satou, C. J. Lin, and T. Ohsawa, *Phys. Rev. Lett.* **93**, 162701 (2004).
- [25] L. R. Gasques, D. J. Hinde, M. Dasgupta, A. Mukherjee, and R. G. Thomas, *Phys. Rev. C* **79**, 034605 (2009).
- [26] S. B. Manohar, A. Goswami, and B. S. Tomar, *J. Radiol. Nucl. Chem.* **203**, 331 (1996).
- [27] A. N. Andreyev, J. Elseviers, M. Huyse, P. V. Duppen, S. Antalic, A. Barzakh, N. Bree, T. E. Cocolios, V. F. Comas, J. Diriken *et al.*, *Phys. Rev. Lett.* **105**, 252502 (2010).
- [28] Mohd. Shuaib, V. R. Sharma, A. Yadav, S. Thakur, M. K. Sharma, I. Majeed, M. Kumar, P. P. Singh, D. P. Singh, R. Kumar, R. P. Singh, S. Muralithar, B. P. Singh, and R. Prasad, *Phys. Rev. C* **99**, 024617 (2019).
- [29] R. Prajapat, M. Maiti, and D. Kumar, *Phys. Rev. C* **103**, 014608 (2021).
- [30] G. K. Gubbi, A. Goswami, B. S. Tomar, A. Ramaswami, A. V. R. Reddy, P. P. Burte, S. B. Manohar, and B. John, *Phys. Rev. C* **59**, 3224 (1999).
- [31] V. R. Sharma, A. Yadav, P. P. Singh, M. K. Sharma, D. P. Singh, Unnati, R. Kumar, K. S. Golda, B. P. Singh, A. K. Sinha, and R. Prasad, *Phys. Rev. C* **84**, 014612 (2011).
- [32] G. S. Karapetyan, A. Deppman, V. Guimaraes, A. Balabekyan, and N. A. Demekhina, *Phys. Rev. C* **94**, 024618 (2016).
- [33] A. Sood, P. P. Singh, R. N. Sahoo, P. Kumar, A. Yadav, V. R. Sharma, Mohd. Shuaib, M. K. Sharma, D. P. Singh, U. Gupta, R. Kumar, S. Aydin, B. P. Singh, H. J. Wollersheim, and R. Prasad, *Phys. Rev. C* **96**, 014620 (2017).
- [34] V. R. Sharma, R. Kumar, S. Mukherjee, E. F. Aguilera, Mohd. Shuaib, P. P. Singh, A. Yadav, R. Dubey, S. Appannababu, J. C. Morales-Rivera, S. Kumar, B. P. Singh, and R. Prasad, *Phys. Rev. C* **99**, 034617 (2019).
- [35] M. de Saint Simon, S. Haan, G. Audi, A. Coc, M. Epherre, P. Guimbal, A. C. Mueller, C. Thibault, F. Touchard, and M. Langevin, *Phys. Rev. C* **26**, 2447 (1982).

- [36] P. Kozma, C. Damdinsuren, D. Chultem, and B. Tumendemberel, *J. Phys. G: Nucl. Part. Phys.* **17**, 675 (1991).
- [37] L. Wenxin, S. Tongyu, C. Tahai, L. Yunsheng, Z. Yuming, S. Ruling, Z. Lili, W. Dingqing, J. Genming, and Sa Benhao, *Phys. Rev. C* **48**, 628 (1993).
- [38] M. Crippa, E. Gadioli, P. Vergani, G. Ciavola, C. Marchetta, and M. Bonardi, *Z. Phys. A* **350**, 121 (1994).
- [39] K. S. Babu, R. Tripathi, K. Sudarshan, B. D. Shrivastava, A. Goswami, and B. S. Tomar, *J. Phys. G: Nucl. Part. Phys.* **29**, 1011 (2003).
- [40] T. D. Thomas, *Phys. Rev.* **116**, 703 (1959).
- [41] A. Gavron, *Phys. Rev. C* **21**, 230 (1980).
- [42] M. Herman, R. Capote, B. V. Carlson, P. Oblozinsky, M. Sin, A. Trkov, H. Wienke, and V. Zerkin, *Nucl. Data Sheets* **108**, 2655 (2007).
- [43] R. Prajapat, M. Maiti, D. Kumar, and A. Chauhan, *Phys. Scr.* **95**, 055306 (2020).
- [44] M. Maiti and S. Lahiri, *Phys. Rev. C* **84**, 067601 (2011).
- [45] M. Maiti and S. Lahiri, *Radiochim. Acta* **99**, 359 (2011).
- [46] D. Kumar, M. Maiti, and S. Lahiri, *Sep. Sci. Technol.* **52**, 2372 (2017).
- [47] D. Kumar, M. Maiti, and S. Lahiri, *Phys. Rev. C* **94**, 044603 (2016).
- [48] J. F. Ziegler, M. D. Ziegler, and J. P. Biersack, *Nucl. Instrum. Methods Phys. Res. B* **268**, 1818 (2010).
- [49] R. Bass, *Phys. Rev. Lett.* **39**, 265 (1977).
- [50] A. J. Sierk, *Phys. Rev. C* **33**, 2039 (1986).
- [51] C. M. Perey and F. G. Perey, *At. Data Nucl. Data Tables* **17**, 1 (1976).
- [52] C. H. Dasso and S. Landowne, *Comput. Phys. Commun.* **46**, 187 (1987).
- [53] R. Capote, M. Herman, P. Oblozinsky, P. G. Young, S. Goriely, T. Belgia, A. V. Ignatyuk, A. J. Koning, S. Hilaire, V. A. Plujko *et al.*, *Nucl. Data Sheets* **110**, 3107 (2009).
- [54] D. Kumar and M. Maiti, *Phys. Rev. C* **95**, 064602 (2017).
- [55] A. Chauhan, M. Maiti, and S. Lahiri, *Phys. Rev. C* **99**, 064609 (2019).
- [56] A. Gilbert and A. G. W. Cameron, *Can. J. Phys.* **43**, 1446 (1965).
- [57] National Nuclear Data Center, Brookhaven National Laboratory, <https://www.nndc.bnl.gov/>.
- [58] S. Y. F. Chu, L. P. Ekstrom, and R. B. Firestone, The Lund/LBNL Nuclear Data Search: WWW Table of Radioactive Isotopes, <http://nucleardata.nuclear.lu.se/toi/>.
- [59] M. Cavinato, E. Fabrici, E. Gadioli, E. Gadioli Erba, P. Vergani, M. Crippa, G. Colombo, I. Redaelli, and M. Ripamonti, *Phys. Rev. C* **52**, 2577 (1995).
- [60] J. Wilczynski, *Nucl. Phys. A* **216**, 386 (1973).
- [61] J. Wilczynski, K. Siwek-Wilczynska, J. V. Driel, S. Gonggrijp, D. C. J. M. Hageman, R. V. F. Janssens, J. Lukasiak, R. H. Siemssen, and S. Y. V. D. Werf, *Nucl. Phys. A* **373**, 109 (1982).